Chitosan-based coatings with tunable transparency and superhydrophobicity: a solvent-free and fluorine-free approach by stearoyl derivatization.

Irene Tagliaro[a]*, Stefano Seccia[a], Beatrice Pellegrini[a], Sabrina Bertini[b], Carlo Antonini[a]*

[a] Department of Materials Science, University of Milano-Bicocca, 20125 Milan, Italy, irene.tagliaro@unimib.it, s.seccia@campus.unimib.it, b.pellegrini4@campus.unimib.it, carlo.antonini@unimib.it

[b] Istituto di Ricerche Chimiche e Biochimiche G. Ronzoni, Carbohydrate Science Department, 20133 Milan, Italy, bertini@ronzoni.it

* Corresponding authors E-mail addresses: irene.tagliaro@unimib.it, carlo.antonini@unimib.it

1

2 **Abstract**

3 One of the current greatest challenges in materials science and technology is the development of safe- and sustainable-
4 by-design coatings with enhanced functionalities, e.g. to substitute fluorinated substances raising concerns for their
5 potential hazard on human health. Bio-based polymeric coatings represent a promising route with a high potential. In
6 this study, we propose an innovative sustainable method for fabricating coatings based on chitosan with modified
7 functionality, with a fine-tuning of coating properties, namely transparency and superhydrophobicity. The process
8 consists in two main steps: i) fluorine-free modification of chitosan functional groups with stearoyl chloride and
9 freeze-drying to obtain a superhydrophobic powder, ii) coating deposition using a novel solvent-free approach through
10 a thermal treatment. The modified chitosan is characterized to assess its chemico-physical properties and confirm the
11 functionality modification with fatty acid tails. The deposition method enables tuning the coating properties of
12 transparency and superhydrophobicity, maintaining good durability.

13 **Keywords**

14 Superhydrophobic coating, chitosan, solvent-free deposition, fluorine-free, transparent, NMR.

1. Introduction

The most recent advances in surface micro- and nano-engineering have propelled the development of synthetic self-cleaning surfaces (Geyer et al., 2020) with superhydrophobic properties, which have a high potential in several industrial application, ranging from efficient heat transfer devices (Donati et al., 2021; Paxson et al., 2014) clean building façades (Asmone & Chew, 2018), drag reduction (Hokmabad & Ghaemi, 2017; Mail et al., 2019; Tanvir Ahmmed & Kietzig, 2016), anti-fouling (M. Wang et al., 2021), anti-bacterial (Jiang et al., 2020; Yin et al., 2019a) and anti-viral surfaces (Jaber et al., 2022). Inspired by natural surfaces, such as the lotus and the Salvinia Molesta leaves (Konrad et al., 2022), superhydrophobic surfaces combine intrinsic hydrophobicity of the superficial layer with nano- and micrometric asperities to obtain superhydrophobicity (Antonini et al., 2013; Eriksson et al., 2019; Maitra et al., 2014; Rioboo et al., 2012), which is macroscopically manifested by high contact angles and low drop roll-off angles. Surfaces are referred to as superhydrophobic if water drops show contact angles higher than 150° (Quéré, 2005) (an arbitrary but normally accepted minimum threshold, although other thresholds in the range of 135-140° have been proposed, based on theoretical considerations (W. Li & Amirfazli, 2005) or experimental results (Antonini et al., 2013; Rioboo et al., 2012), and low contact angle hysteresis (Eral et al., 2013; Lafuma & Quéré, 2003), typically lower than 5-10°. Due to surface topography and chemistry, air is trapped at the substrate-water interface, reducing the effective contact area and thus liquid adhesion (Butt et al., 2014; Milne & Amirfazli, 2009); simple equations, e.g. the so-called Cassie-Baxter equation (Milne & Amirfazli, 2012), can be used to estimate the effective contact angle on a superhydrophobic surface.

The bio-inspired tuning of surface chemistry and topography by surface engineering has proved to be successful for developing superhydrophobic coatings. The use of fluorinated materials remains so far the most effective route, due to the intrinsic hydrophobicity of perfluorinated compounds (Muñoz-Bonilla et al., 2010; Teisala & Butt, 2019; Vilaró et al., 2017). However, there is an urgent need to identify alternatives, due to rising safety and environmental concerns, which has, for example, recently led in EU to the ban of Perfluorooctanoic acid (PFOA). In 2017 (Commission Regulation (EU) 2017/1000 of 13 June 2017 Amending Annex XVII to Regulation (EC) No 1907/2006 of the European Parliament and of the Council Concerning the Registration, Evaluation, Authorisation and Restriction of Chemicals (REACH), 2017), PFOA has been included in the EU REACH regulation as "persistent, bioaccumulative and toxic" and has been banned under the EU's Persistent Organic Pollutants Regulation since 2020 (Commission Delegated Regulation (EU) 2020/784 of 8 April 2020 Amending Annex I to Regulation (EU) 2019/1021 of the

43　European Parliament and of the Council as Regards the Listing of Perfluorooctanoic Acid (PFOA), Its Salts and

44　PFOA-Related Compounds, 2020). Very recently, (Caporale et al., 2022) it was found that exposure in early pregnancy

45　to an endocrine disrupting chemical mixture, including perfluoroalkyl substances, is associated with language delay

46　in offspring. Moreover, perfluorinated compounds are long lasting chemicals, which do not biodegrade, posing severe

47　consequences for the environment and for human health. As an example, industrial wastes may contaminate the soil

48　and expose agricultural fields to pollution, as well as the groundwater, poisoning the drinking system of entire regions,

49　as it happened in the north-east region in Italy[1], over an area of more than 1000 km^2. In 2021, the European Drinking

50　Water Directive introduced a limit of 0.5 µg/l for perfluorinated chemicals (Position (EU) No 14/2020 of the Council

51　at First Reading, 2020). As such, superhydrophobic safe and sustainable alternatives based on natural waxes (Ostrov

52　et al., 2019; Wan et al., 2021), rice husk (Junaidi et al., 2016; Long et al., 2022) and starch (Ghasemlou et al., 2021;

53　Meng et al., 2022; F. Wang et al., 2021) from biomass and agricultural waste (D. Li et al., 2020; Ren et al., 2021; Seth

54　& Jana, 2022) have become highly desirable. Materials can be functionalized with fluorine-free non-polar moieties

55　for producing hydrophobic coatings. Fatty acids, such as stearic acid, have been exploited as modifiers of functionality

56　due to their long and saturated alkyl tails which, which promote water repellency similar to fluorinated tails (Heale et

57　al., 2018; Q. Wang et al., 2008; Yang et al., 2010).

58　Moreover, the combination of safe and environmental-friendly raw materials with simple and sustainable deposition

59　processes is challenging, since the hydrophobized biopolymers are usually hard to redisperse in harmless solvents (X.

60　Chen et al., 2022), once modified in their functionality. It is thus important to look for solvent-free strategies, as

61　chemical vapor deposition approaches (Paxson et al., 2014; Soto et al., 2018) and thermoplastic polymer or prepolymer

62　mixtures deposition (J. Huang et al., 2021; Z. Huang et al., 2019; Liu et al., 2019; Zhang et al., 2014) (although this

63　class of materials are normally non-biodegradable). The most common eco-friendly film preparation techniques

64　involve the use of water or ethanol (Bayer, 2020; Zhao et al., 2019), but require the achievement of a stable dispersion

65　of particles (Divandari et al., 2021), which is hard to obtain with molecules bearing non-polar tails. Also, in many

66　real-world applications, superhydrophobicity and transparency are both required properties; however, it is difficult to

67　obtain them simultaneously due to conflicting requirements: the roughness needed to promote superhydrophobicity is

---

[1] https://rdv.app.box.com/s/0agk48tvcxdis53m6ud9ccjfwnbbdgyi

68   detrimental to transparency, due to light scattering. Indeed, the Mie scattering of visible light (ca. 380–760 nm) impacts

69   negatively on the transparency in the presence of features of a comparable wavelength (Levkin et al., 2009).

70   To address this problem of combining functional properties, polysaccharides, such as cellulose and chitosan, are

71   appealing substrates because of their good filming (Madeleine-Perdrillat et al., 2016) and mechanical properties

72   (Khodayari et al., 2020, 2021; Zhu et al., 2015) and potential transparency (Cazón et al., 2017; Fernandes et al., 2009;

73   Ladiè et al., 2021; Yin et al., 2019b, 2021). Among polysaccharides, chitosan is commercially available as a renewable

74   source from the shellfish industry, derived from chitin (second most abundant polysaccharide in nature) from

75   crustacean wastes (Cazón et al., 2017; Muñoz et al., 2018). Chitosan demonstrates selective gas permeability (Morin-

76   Crini et al., 2019) as edible coating for food preservation (Duan et al., 2019; Rayees et al., 2013), maintaining

77   nutritional quality, inhibiting microorganism growth (Han et al., 2022) and preventing contamination: thus, it is

78   emerging for its high-potential to substitute oil-based plastics. Chitosan is a linear polysaccharide copolymer

79   consisting of β-(1-4)-2-acetamido-D-glucose and β-(1-4)-2-amino-D-glucose units (β-(1-4)-2-amino-D-glucose units

80   more than 50% and less than 98%, usually 75 - 80%). Each glucose unit possesses one amino (or acetamido) and two

81   hydroxyl groups, which determine on one side a hydrophilic nature, but also enable the introduction of different

82   functionalities (Fink et al., 2009; Geissler et al., 2013; Rinaudo, 2006; S. Wang et al., 2018; Yazdani-Pedram et al.,

83   1995).

84   Within this framework, the latest most interesting works based on polysaccharide materials were not able to combine

85   both transparency and superhydrophobicity on the same coating (Geissler et al., 2013; Tang et al., 2021; S. Wang et

86   al., 2018), without the exploitation of perfluorinated chemicals (L. Chen et al., 2014; J. Huang et al., 2018; Morrissette

87   et al., 2018), whose application damp the benefits of using safe natural substances from renewable sources. To exploit

88   the potential of polysaccharide for fabrication of superhydrophobic coatings, versatile, safe and environmentally

89   sustainable preparation methods are needed. Here we report a simple method to fabricate chitosan-based fluorine-free

90   surfaces with the goal of tuning transparency and superhydrophobicity. The process consists of two main steps of

91   chitosan functionality modification and solvent-free deposition. This process finds a good balance of deposited coating

92   morphological structuring to impart transparency and superhydrophobicity through optimal tuning. Although the

93   chemical functionalization makes use of a non-environmentally friendly solvent (namely pyridine, non-replaceable

94   solvent as acid scavenger in reaction involving acyl chlorides), the proposed solventless deposition method addresses

95   the requirements of environmental sustainability, restricting the use of solvents during the particle functionalization

96 and avoiding the solvent handling of the end-user. Moreover, the combination of fatty acid chains with the structure

97 of a biopolymer may pave the way to a biodegradable material (although this is out of the scope of this study).

98 **2.   Materials and methods**

99 2.1. Materials

100 Chitosan powder (DD 80%, M_W 230,000, CAS 9012-76-4), Stearoyl Chloride (97%, CAS 112-76-5), and Pyridine

101 (≥99%, CAS 110-86-1) in analytical grade were purchased from Sigma-Aldrich and used as received.

102 Dichloromethane stabilized with 0.2% v/v of ethanol (DCM, CAS 75-09-2) and Ethanol absolute (EtOH, CAS 64-17-

103 5) were purchased from VWR Chemicals BDH. For enzymatic digestion, lysozyme (CAS 9001-63-2) was purchased

104 by Sigma-Aldrich.

105 2.2. Chitosan functionality modification

106 The functionality modification reaction is performed on pristine chitosan with M_W 230 kDa (assessed by high

107 performance size exclusion chromatography with a triple detector array HP-SEC-TDA and confirmed by Dynamic

108 Light Scattering DLS) and a deacetylation degree of 80%, as illustrated in Fig. S1, S2 in the Supporting Information.

109 Before the reaction, chitosan is stored at 70°C overnight to dry the product and lower the presence of adsorbed water.1

110 g of dried chitosan is added to 60 ml of pyridine in a 250 ml reaction flask. The reagents are heated at 115°C and 13.2

111 ml of stearoyl chloride are added. The reaction is kept at 115°C under reflux for 5 hours so that stearoyl chloride reacts

112 with hydroxide and amine groups of chitosan via esterification and amidation, respectively. After the reaction has

113 cooled down, the product is filtered and washed with 100 ml of EtOH. The as obtained modified chitosan undergoes

114 washing cycles for assuring the elimination of unreacted products, with increasing volume of solvents to assure the

115 complete elimination of stearoyl chloride. The cycles consist in dissolution of modified chitosan in 100 ml of DCM,

116 precipitation with 100 ml of EtOH and filtration by Buchner funnel. This procedure is repeated three times. The

117 modified chitosan is further purified by 3 additional cycles of dispersion (30 mg of modified chitosan dispersed in 25

118 ml of DCM) and reprecipitation (150 ml of EtOH), followed by centrifugation at 9000 rpm for 10 minutes. After

119 reprecipitation, the product color turns from brown to white. The reprecipitated modified chitosan is dispersed in 100

120 ml of DCM and frozen with liquid nitrogen in small aliquots of 10 ml. The product is dried in a vacuum desiccator

121 for 2 hours. The freeze-drying produces a white fine powder. The resulting modified chitosan powder is easy to store

122 for long time and, if needed, to redisperse in appropriate solvents.

123   2.3. Solvent-free deposition

124   The ChiSt (Chitosan modified with Stearoyl chain) powder is sieved through a 100 µm steel mesh and deposited in a

125   compact layer over a glass slide. The procedure of powder spreading over the surface is performed with the use of a

126   big sieve (10 x 15 cm) on top of a small glass slide (2.5 x 2.5 cm). The powder is spread by a random process and the

127   homogeneity of the coverage is assessed a posteriori by measuring the average thickness of the coating. The substrates

128   are then treated in the oven for 10 min at 150°C. This procedure can be easily applied on solid large substrates which

129   do not degrade at high temperature and does not require any solvent. The mechanism of particle adhesion to the

130   substrate is due to the increase of viscosity which make ChiSt particles coalesce and conformally adapt and anchor to

131   the asperities of the substrate.

132   2.4. Characterization analyses

133   Measurements for molecular weight distribution of chitosan were performed on a Viscotek 302 HPLC system

134   (Malvern Instruments LtD, Malvern, UK). The array exploits simultaneous action of Refraction Index (RI),

135   Viscometer, Right Angle Laser Light Scattering (RALS) and Low Angle Light Scattering (LALS) detectors. To

136   prepare the solutions for HP-SEC-TDA measurements, 60 mg was dissolved in the mobile phase volume, to obtain a

137   sample concentration of ~6 mg/ml. The chitosan solution was stirred for 24h and then diluted in a mobile phase to a

138   concentration of ~1 mg/ml. The analysis was performed at 30° C, using 1 x TSKPWXL column (Tosoh Bioscience,

139   7 mm 7.8 × 30 cm). A solution of AcONa 0.3M/AcOH 0.3M containing 0.05% NaN_3, prefiltered using 0.22 mm filter,

140   was used, with a flow rate of 0.6 ml/min. Results are reported in Figure S1 and Table S1. Chromatographic profiles

141   were elaborated using the OmniSEC software version 4.6.2. RI increments, referred to as dn/dc, were imposed 0.163

142   mg/ml to enable conversion of RI values into a concentration.

143   DLS to assess the Chitosan molecular weight was performed using the Zetasizer Nano ZS (Malvern, Worcestershire,

144   United Kingdom) with a fixed scattering angle of 173° and a 633-nm helium–neon laser. Data were analyzed using

145   Zetasizer software version 7.11 (Malvern, Worcestershire, United Kingdom). For size analyzes, solutions of 1 mg/ml

146   were prepared solubilizing Chitosan in AcONa 0.3M/AcOH 0.3M. Results are reported in Figure S2.

147   The ChiSt ^{1}H NMR spectra are obtained with a Bruker AVANCE IIIHD 500 MHz spectrometer (Bruker, Karlsruhe,

148   Germany) equipped with a 5 mm BBO probe, at 298 K. Spectra are processed with Bruker Topspin software version

149   4.10.16. Approximately 30 mg of sample are dissolved in 3 mL of Chloform-d ($CDCl_3$) with 0.03 %TMS with 0.6

150   mL transferred into a 5 mm NMR tube (Bruker, Karlsruhe, Germany). For the calculation of the degree of substitution,

151   an enzymatically digested ChiSt sample is analyzed by ^{1}H NMR with a Bruker AVANCE NEO 500MHz spectrometer

152   (Bruker, Karlsruhe, Germany) equipped with a 5 mm TCI cryogenic probe at 298 K. Approximately 20 mg of sample

153   are dissolved in 0.6 mL of Chloform-d (CDCl$_3$) with 0.03 %TMS transferred into a 5 mm NMR tube (Bruker,

154   Karlsruhe, Germany). ^{1}H NMR spectra are acquired with in sequence, using 16 scans, 12 s relaxation delay, and a

155   number of time-domain points equal to 32k; data are processed with Bruker Topspin software version 4.10.16.

156   The ChiSt ^{13}C-DD-MAS solid state NMR spectra are obtained with a Bruker AVANCE IIIHD 500MHz spectrometer

157   (Bruker, Karlsruhe, Germany) equipped with a 3.2 mm CPMAS probe, at 298 K.

158   To calculate the degree of substitution by NMR analysis, a enzymatic degradation procedure has been performed on

159   ChiSt (Ladiè et al., 2021; Stokke et al., 1995). For enzyme solution preparation, approximately 150 mg of lysozyme

160   was dissolved in 2 ml of deionized H$_2$O and stirred for 1 h (75 mg/ml). 40 mg of ChiSt were dispersed in 2 ml of

161   enzyme solution, the heterogeneous solution was stirred at 38°C in an oil bath. After 48 h the solution was centrifugated

162   (3000 rpm, 10') and filtered to recovery the water insoluble hydrolyzed product (cut off 0.20 μm). The product was

163   washed with cold deionized water and finally recovered by lyophilization. Since the product is insoluble in water, at

164   the end of the hydrolysis, the absence of the polysaccharide component in the supernatant was verified by NMR

165   spectroscopy and colorimetric assay, confirming the homogeneity of substitution of chitosan chains and consequently

166   of hydrolyzed product.

167   The infrared spectra are analyzed through attenuated total reflection-Fourier transform infrared spectroscopy (ATR-

168   FTIR) by a Perkin Elmer Spectrum 100 instrument (Perkin Elmer,Waltham, MA, USA) (4 cm^{-1} resolution, 650–4000

169   cm^{-1} range, 8 scans).

170   The thermogravimetric analysis (TGA) is performed with a Mettler Toledo TGA/DSC1 Star-e System. The variation

171   of weight is analyzed by heating from 30 to 1000 °C, at 5°C/min, under an air flux of 50 ml/min.

172   The contact Angle analysis is performed using an in-house contact angle setup, consisting of a camera (Fastcam Nova

173   S6, Photron) with Tokina AT-X PRO D (100 mm F2.8 MACRO) as optical lens and backlight illumination.

174   Advancing, θ_A, and receding, θ_R, contact angles, as well as the contact angle hysteresis, $\Delta\theta=\theta_A-\theta_R$, are measured

175   dispensing and withdrawing water with a syringe pump (Harvard Apparatus, Pump 11 Pico Plus Elite) at a rate of 10

176   μl/min, with drop volumes in the range of 5-10 μl.

177 Morphology of ChiSt coatings is investigated by Scanning Electron Microscopy (SEM) analysis, performed by a Vega

178 TS5136 XM Tescan microscope (Tescan Brno s.r.o., Kohoutovice, Czech Republic). The electron beam excitation is

179 30 kV at a beam current of 25 pA, and a working distance of 12 mm. Prior to SEM analysis, samples are gold-sputtered.

180 ImageJ processing program (Image Processing and Analysis in Java, Version No 2, National Institutes of Health,

181 Bethesda, MD, USA) is used to measure the coating morphological features.

182 The transparency is assessed by UV-Vis analysis with a Agilent Technology Cary 60 UV-Vis. The spectra are

183 performed at medium speed, in the 200-800 nm range, in dual beam mode.

184 The optical microscope used for this research is a Leica Microsystems DM/LP equipped with 5 lens from 5x to 1000x.

185 The durability of the coatings a tested by different approaches: i) abrasion resistance test, ii) resistance in water and

186 acid environment; iii) adhesion tape test. The abrasion resistance test is performed using sandpaper (800 grit) and a

187 100 g weight. The coated glass slide is placed face down on the sandpaper with the 100g weight loaded on top with a

188 total pressure over area of 1.6 kPa. The glass slide is then dragged for 3 cm over the sandpaper. This procedure is

189 repeated 10 times to reach a cumulative abrasion length of 30 cm. After each step (i.e. 3 cm), contact angle

190 measurements are performed to monitor the evolution of the wetting properties.

191 The coatings have been tested in their resistance to water and acidic environment. The samples are immersed in

192 distilled H_2O for 5 h and in a solution at pH 2 (HCl 37%, 1 ml diluted in 200 ml H_2O) for 2 h and dried in the air.

193 These procedures are repeated for 5 cycles, after which contact angle measurements are performed.

194 The adhesion has been assessed by ISO standard adhesive tape test (EN ISO 2409). This procedure consists in tape

195 application on the sample, pressing and rubbing to ensure adhesion and tape peel off from the sample. The contact

196 angle variations are monitored over 10 cycles of tape applications.

197 Each measurement is averaged over 5 samples repetition.

198 **3. Results and Discussion**

199 3.1. Chitosan functionality modification and solvent-free deposition strategy

200 To fabricate a chitosan-based coating with tunable hydrophobicity and transparency (Fig. 1) , the process includes two

201 major steps (Fig. 1a): (i) chitosan backbone functionality modification, and (ii) solvent-free deposition. The first step

202 exploits the esterification and secondary amide formation reaction of stearoyl chloride, which reacts with hydroxyl

203   and amine groups on the chitosan backbone (S. Wang et al., 2018). The reaction is performed in pyridine, which act

204   as HCl scavenger, by-product of esterification and amidation (Ouellette & Rawn, 2018). After washing cycles, the

205   reaction product, ChiSt, is freeze-dried. In this process, the solvent nucleates and concentrates ChiSt in the regions

206   between the forming crystals. After freezing is completed, the solvent is removed via sublimation, obtaining an open

207   porous morphology, which result in a dry powder.
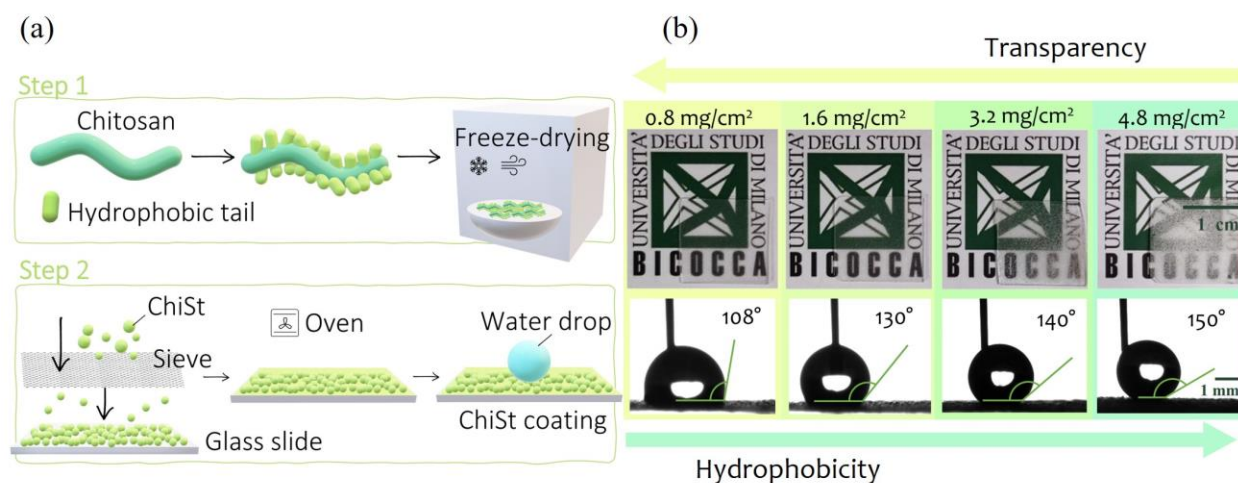
208

209   **Fig. 1.** (a) Schematics of the chitosan functionality modification and coating preparation. (b) Contact angle

210   measurements (θ_A) and pictures of coatings with increasing amount of ChiSt per area.

211

212   Freeze-dried ChiSt appears as a fine white powder, which shows superhydrophobic properties (Video SV1 in the

213   Supporting Information). The superhydrophobic characteristic of the powder is evident with a simple test, in which

214   the finger skin covered with ChiSt becomes superhydrophobic: when the finger is immersed in water, the skin appears

215   transluncent, due to plastron (i.e. air layer at the skin-water interface) formation, and remains dry. Freeze-dried ChiSt

216   can be safely stored and effectively transported, due to the solvent removal, and avoiding undesired ChiSt aggregation,

217   usually observed during oven drying.

218   In the second step, ChiSt powder is sieved with a 100 µm-pore mesh over a glass slide and anchored to the substrate

219   by a heat treatment in the oven (Fig. 1a). This deposition method is innovative as, to the best of our knowledge, it was

220   never applied in the field of polysaccharide-based films. The method exploits the temperature treatment for sintering

221   ChiSt particles and forming a coating. Particles are heated slightly above the material T_g, which is enough to promote

222   particle-particle cohesion and particle-substrate adhesion.

223   During deposition, the amount of ChiSt can be controlled to obtain films with variable properties. As visible in Fig.

224   1b, using ChiSt in the range 0.8 and 4.8 mg/cm^2, hydrophobicity increases with increasing ChiSt amount, as advancing

225   contact angles θ_A raise from 108° to 150°, thus reaching a superhydrophobic state. Conversely, transparency visibly

226   follows the opposite trend and decreases when increasing ChiSt amount. These results are not presented in comparison

227   to films made of bare chitosan because any pristine chitosan coating swells immediately as soon as the drop touches

228   the surface, making the contact angle analysis impossible to perform.

229   In the next section, we provide the details on material and film characterization, to explain these results and identify

230   a potential optimum for the design of a chitosan-based coating possessing both hydrophobicity and transparency.

231   3.2. Modified chitosan characterization

232   ChiSt is characterized by chemico-physical analysis using ^{1}H, ^{13}C DD-MAS Solid State NMR, FTIR and TGA to

233   assess the effective modification of functionalization of the chitosan backbone.

234   Fig. 2a shows the ^{1}H NMR spectrum of ChiSt (S. Wang et al., 2018). The major chemical shifts between 0.5 ppm and

235   2.6 ppm are attributable to the hydrogens of the stearoyl aliphatic chains and of the chitosan H-Ac groups. Peaks in

236   the range 3.0 ppm to 4.7 ppm are attributable to the protons of the chitosan polymer backbone, except for the anomeric

237   protons with peaks between 5 ppm and 6 ppm. To determine the substitution degree, the ^{1}H NMR spectrum of the

238   hydrolyzed ChiSt by enzymatic digestion has been acquired (Fig. S3). By lysozyme hydrolysis(Ladiè et al., 2021), the

239   sample presents the same chemical structure but reduced molecular weight of ChiSt; using this analytical strategy, it

240   is possible to obtain a more resolved spectrum, due to the decreases of signals width, and more homogeneous protons

241   relaxation times of chitosan backbone respect to the substituent protons.
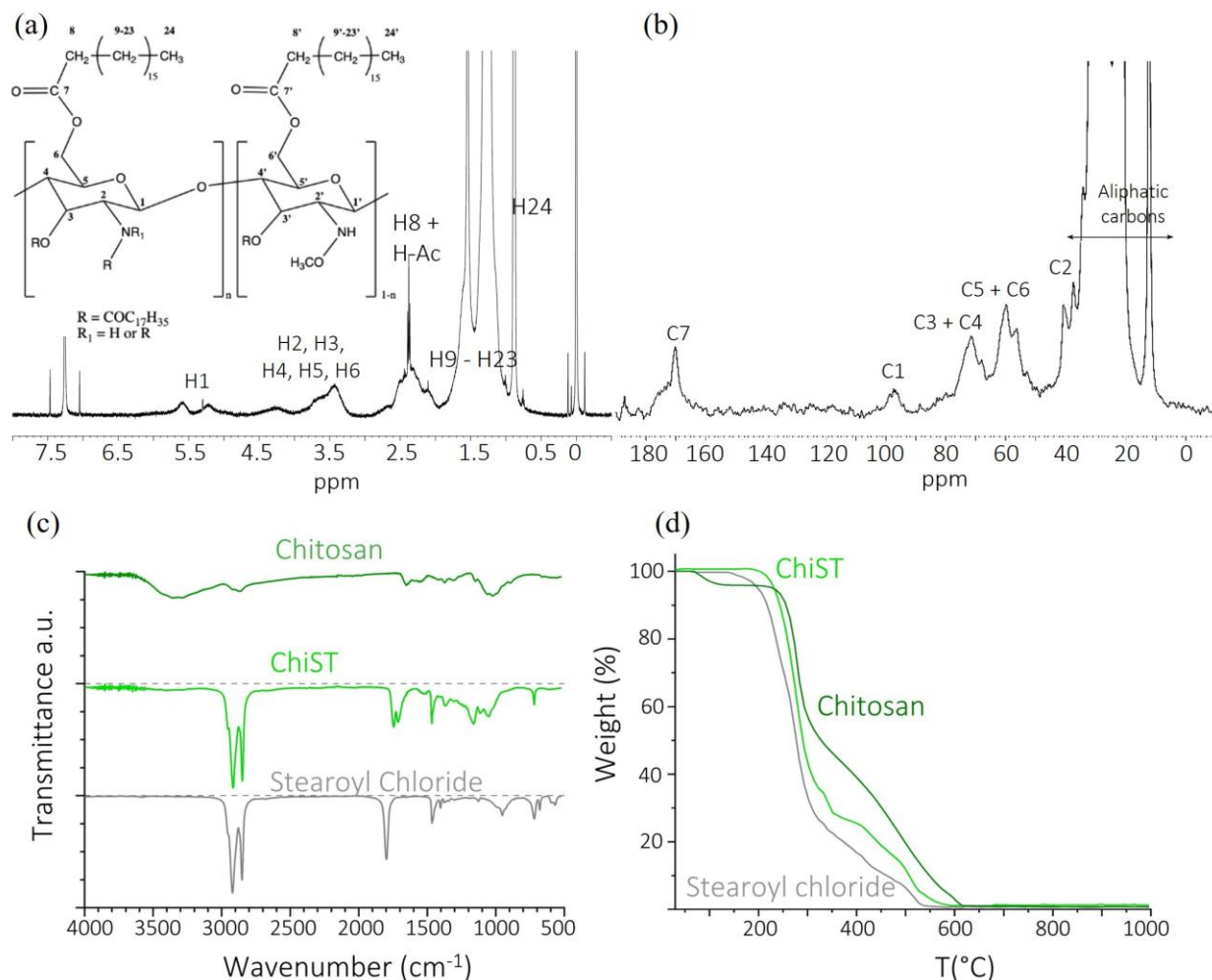
Fig. 2. (a) ^{1}HNMR of ChiSt. (b) ^{13}C DD-MAS Solid State NMR of ChiSt. (c) FTIR of chitosan (dark green line), ChiSt (light green line) and stearoyl chloride (grey line). (d) TGA analysis of chitosan (dark green line), ChiSt (light green line) and stearoyl chloride (grey line).

Both aspects favor quantification by NMR spectroscopy. In particular, by integrating the signal related to H24 compared to the signals related to the hydrogens of the chitosan polymeric backbone, a degree of substitution of ~70% is determined (^{1}H-NMR analysis in Fig. S3).

The ^{13}C DD-MAS Solid State NMR spectrum of ChiSt is reported in Fig. 2b. The major chemical shifts at 12 ppm, and 20 ppm to 43 ppm, are attributable to the carbon atoms composing the stearoyl chains, particularly the terminal methyl groups and the aliphatic methylene groups, respectively. The chemical shifts observed between 50 ppm and 100 ppm are assigned to the carbon atoms composing the chitosan polymeric backbone: C2 at 40 ppm, C5/C6 at 57 ppm to 62 ppm, C3/C4 at 70 ppm to 73 ppm, and C1 at 98 ppm. Finally, the peak at 170 ppm is attributed to different

254 components: the sharp peak at high fields to the amide group of the chitosan (Saber-Samandari et al., 2012)and the

255 shoulder at low fields to the ester of ChiSt (S. Wang et al., 2018; Zong et al., 2000).

256 In Fig. 2c, FTIR spectra of ChiSt are compared with those from pristine chitosan and stearoyl chloride. The main

257 vibration bands of chitosan are identified by the broad peak at around 3400 cm^{-1}, corresponding to hydroxyl and amine

258 stretching modes, and around 2900 cm^{-1}, corresponding to C-H symmetric and asymmetric stretching, a common

259 fingerprint for polysaccharides. The absorption peaks at around 1645 cm^{-1} and 1325 cm^{-1} are attributed to stretching

260 vibrations of carbonyls of the N-acetyl groups along the copolymer chain, while at 1066 cm^{-1} and 1028 cm^{-1} the C-O

261 stretching modes appear (Queiroz et al., 2015). Stearoyl chloride shows major absorption peaks at 2918 cm^{-1} and 2847

262 cm^{-1}, corresponding to the aliphatic C-H group stretching vibrations, while rocking and bending vibrations are found

263 at 1466 cm^{-1}, 718 cm^{-1} and 678 cm^{-1}. 1799 cm^{-1} corresponds to the carbonyl vibrations in the -COCl group (Alkan et

264 al., 2012).

265 Comparing FTIR spectra of the pristine chitosan with ChiSt, a significant decrease in stretching vibration intensity of

266 hydroxyl and amine groups is visible at 3400 cm^{-1}, suggesting both these groups have been involved in the reaction

267 with stearoyl chloride (S. Wang et al., 2018). Furthermore, the carbonyl absorption peak in the acyl group at 1799 cm^{-1}

268 ^{1} shifts and splits into two peaks, 1711 cm^{-1} and 1747 cm^{-1}, assigned to carbonyls of -NCOR and -COOR groups,

269 respectively, further confirming the esterification reaction and secondary amide formation. The main vibration modes

270 of the chitosan backbone and of the stearoyl aliphatic chains are preserved.

271 The thermogravimetric analysis of ChiSt is showed in Fig. 2d with a comparison of the pristine reagents. Up to 150°C,

272 a first weight loss is related to water desorption, which is higher for pristine chitosan (4%), in agreement with the

273 presence of hygroscopic hydroxyl groups measured by FTIR analysis. The major weight loss appears between 150°C

274 to 600°C (96%), bringing to complete degradation, as expected for organic samples. For all samples, degradation has

275 two steps, the first in the range 150-350 °C, the second in the range 350-600 °C. In these regions, the oxidation of the

276 organic component is followed by decomposition of oxidized molecules. The high weight losses are attributed to

277 carbon chain scission with the formation of volatile degradation products. Differently from pristine chitosan, ChiSt

278 does not show any water desorption, i.e. no hygroscopicity, and its degradation starts at an intermediate temperature

279 between chitosan and stearoyl chloride, further confirming that ChiSt is not a simple a mixture (Zawadzki &

280   Kaczmarek, 2010). Indeed, the combined chemico-physical characterization of ChiSt via NMR, FTIR and TGA

281   provides consistent indication of chitosan functionality successful modification with stearoyl chains.

282   Fig. 3 shows SEM analysis of the ChiSt freeze-dried powder at different magnifications and reveals that the particles

283   size is compatible with the pore mesh size (100 µm). The ChiSt freeze-dried powder is structured as aggregates of

284   lamellar sheets with layers of the order of hundreds of nm. This highly structured shape of the lamellar particles is

285   compatible with the obtainment of superhydrophobic properties when spread over surfaces, i.e. a finger (Video 1 in

286   the Supporting Information).
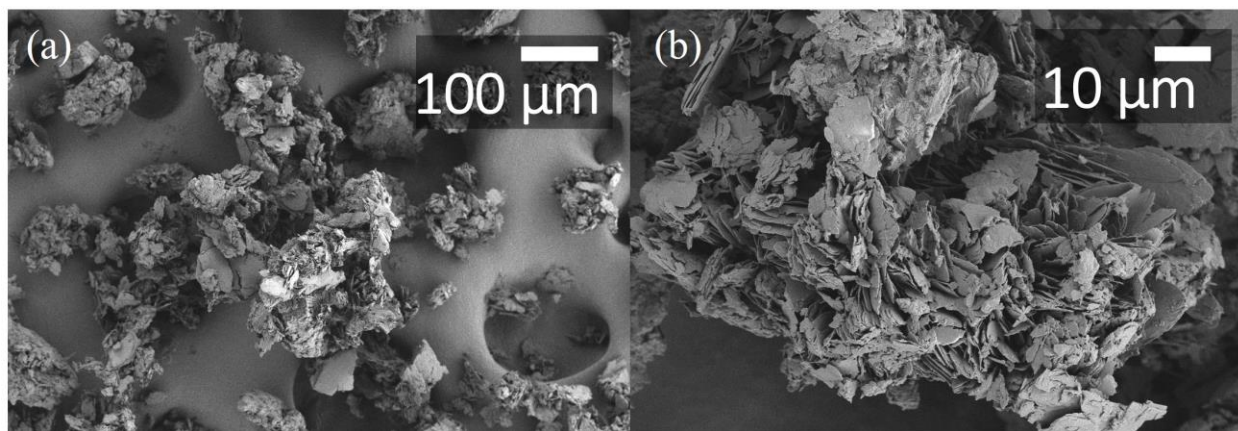
287

288   **Fig. 3.** SEM analysis of freeze-dried ChiSt particles sieved over a 100 µm mesh.

289   3.3. Chitosan-based Coating characterization

290   Different ChiSt samples have been prepared varying the deposited ChiSt amount, with values ranging from 0.8 to 4.8

291   mg/cm^2. Film characterization is then performed to evaluate wetting and optical properties, by means of sessile drop

292   contact angle testing and UV-Vis transmission (Fig. 4b).

293
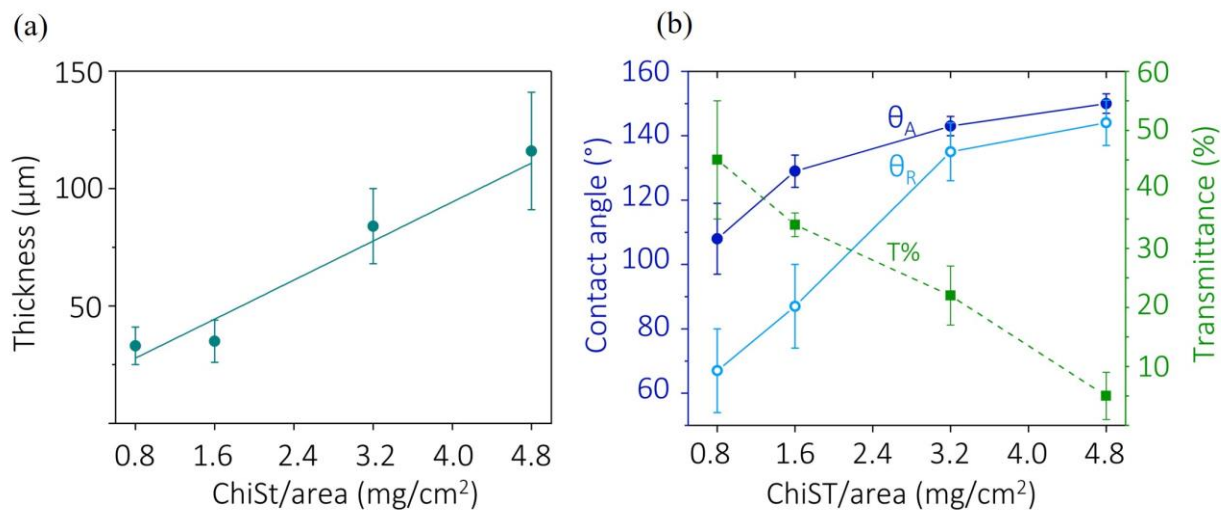
Fig. 4. (a) Thickness of coatings, evaluation by SEM analysis with linear fitting. (b) Quasi-static contact angle analysis

of ChiSt coatings: θ_A advancing angle (blue closed circles), θ_R receding angle (light blue open circles) and UV-Vis

transmittance percentage (green squares).

As shown in Fig. 4a, the thickness of coatings obtained by the deposition of different amounts of ChiSt amount/area

increases linearly. 0.8 mg/cm^2 corresponds to 33 µm ± 8, 1.6 mg/cm^2 to 35 µm ± 9, 3.2 mg/cm^2 to 84 µm ± 16, 4.8

mg/cm^2 to 116 µm ± 25 (Fig. S5). Overall, we have obtained an apparent density between 0.23 g/ml and 0.49 g/ml.

In Fig. 4 b, the advancing, θ_A, and receding, θ_R, contact angles are presented as a function of ChiSt amount (expressed

as mass per unit area). For ChiSt low amount the coating is mildy hydrophobic ($\theta_A = 108° \pm 11°$, $\theta_R = 67° \pm 13°$ for

0.8 mg/cm^2) with relatively high hysteresis, whereas for ChiSt high amount the coating becomes superhydrophobic

($\theta_A = 150° \pm 3$, $\theta_R = 144° \pm 7°$, for 4.8 mg/cm^2). Increasing the amount of ChiSt, thus, leads both to an increase of the

contact angles values and to a decrease of hysteresis, $\Delta\theta$, from $41° \pm 17°$ to $7° \pm 6°$, increasing water drop mobility on
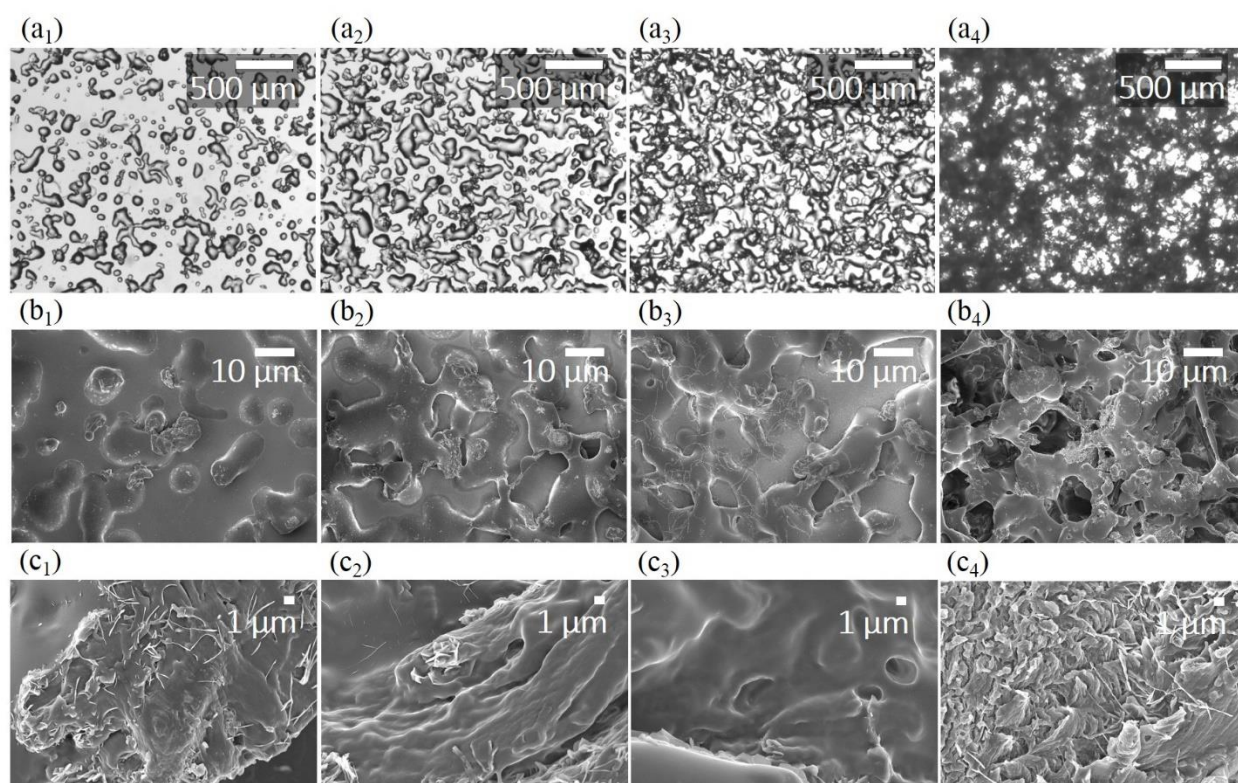
the surface.

UV-Vis transmittance measurements, also illustrated in Fig. 4b, show a decrease in transparency for increasing ChiSt

amount. Samples with 4.8 mg/cm^2, which show superhydrophobic behavior, present a significant decrease of

transmittance to 5% ± 4%, considering that the transmittance of bare glass is 98%.

Transparency increases at 3.2 mg/cm^2 to 22% ± 5% and at 1.6 to 34% ± 2%, and the highest transparency of 45%

±10% is obtained for 0.8 mg/cm^2. The complete UV-Vis spectra (see Fig. S4 of the Supporting Information) show

311   that the transmittance is constant over most of the radiation spectrum (380 to 800 nm) as there is no specific absorption

312   peaks, with a significant decrease of transmittance below 380 nm due to the glass substrate (Ajadi et al., 2016).

313   To investigate the occurrence of any degradation of the polymer backbone after the thermal treatment at 150°C, we

314   performed TGA and DSC analysis (Fig. S6 and S7). Comparing the curves before and after the treatment we do not

315   identify any significative modification, confirming the absence of thermal degradation of the polymer structure.

316   To better understand the correlation between surface topography and the macroscopic wetting and transmittance

317   properties, coatings were analyzed using optical microscopy (Fig. 5a) and SEM (Fig. 5b-c).

318

Fig. 5. Optical microscope analysis of: (a_1) 0.8, (a_2) 1.6, (a_3) 3.2, (a_4) 4.8 mg/cm^2, and the corresponding SEM images (b_1 to b_4 and c_1 to c_4) at higher magnifications.

321   For 0.8 mg/cm^2 (Fig. 5a_1-b_1-c_1), the surface is only partially coated by ChiSt, which is distributed in islands in the

322   range 30-150 µm, comparable to the ChiSt powder characteristic size (Fig. 3). The original lamellar shape obtained

323   by the freeze-drying process (Fig. 3) is partially lost thanks to the overtake of the material's T_g, which allowed to

324   ChiSt to relax over the surface and anchor to the substrate. The partial coating makes the surface heterogeneous with

325   hydrophilic (glass) and hydrophobic (ChiSt) patterns, which is consistent with the high $\Delta\theta$ obtained for this sample,

326   due to a low θ_R connected to contact line pinning in the de-wetting phase. By increasing ChiSt to 1.6 mg/cm^2 (Fig.

327   5a$_2$-b$_2$-c$_2$), ChiSt islands reach larger sizes of ~ 200 – 300 µm, due to merging of particles; however, the glass is still

328   partially coated. At 3.2 mg/cm^2 (Fig. 5a$_3$-b$_3$-c$_3$), ChiSt organizes itself in areas of around 500 µm with increased

329   topographical complexity. This intermediate state of coated and uncoated areas allows to simultaneously obtain a

330   superhydrophobic surface combined with 25% transmittance (Fig. 1b). For 4.8 mg/cm^2 (Fig. 5a$_4$-b$_4$-c$_4$), the coating

331   becomes more compact, whilst preserving a microscale roughness (with structures and pores of the order of 10-100

332   µm, see Fig. 5b$_4$): the structure and the coverage enable on one hand to reach a superhydrophobic wetting state, but

333   on the other hand drastically reduce light transmittance. Closer magnification of the coatings (Fig. 5c$_1$, c$_2$, c$_3$, c$_4$)

334   reveals the characteristic fibrous like shape of chitosan, already analysed elsewhere (Ladiè et al., 2021a). The

335   characteristic fibrous-like shape of chitosan, which is found with higher density at high ChiSt mg/cm^2 (Fig. 5c$_4$),

336   increases the roughness at a length scale of the order of 100 nm. This fragmented aspect provides a dual scale

337   roughness that promotes superhydrophobicity.

338   The observed morphology is a direct effect of the solvent-free deposition strategy, where the thermal treatment

339   promotes adhesion to the substrate. The thermal treatment aims at anchoring ChiSt powder to the glass surface when

340   temperatures approach the glass transition temperature, T_g. Despite difficulties in assessing the T_g for chitosan, which

341   are related to the biopolymer hygroscopicity, a value of 150°C has been measured (Dong et al., 2004). The glass

342   transition has been related to α-relaxation, which is linked to the motion of segments in the main chain, whereas no

343   correlation was found with the β-relaxation, which involves the side groups that depends on the deacetylation degree

344   (80% in our samples)(Dong et al., 2004). At temperatures close to T_g, ChiSt behaves as a non-glassy viscous-liquid

345   polymer: as such, the increased molecular mobility promotes both cohesion between particles and adhesion with the

346   glass substrate, leading to the formation of a coating.

347   By changing ChiSt amount on the surface, the corresponding coating morphology modification impacts both

348   wettability and transparency. A strong decrease in transparency is, indeed, the result of a highly structured and more

349   compact material (4.8 mg/cm^2 sample) which, on the other side, shows remarkable superhydrophobicity. A low

350   structural organization and a lower surface coverage correspond to highly transparent films with loss of

351   superhydrophobicity (0.8 mg/cm^2 sample), and increase of capillary adhesion (higher hysteresis).

352 As such, a good balance of nearly-transparent and superhydrophobic surface, based on the qualitative assessment in

353 Fig. 1 and the quantitative results in Fig. 4, can be identified for ChiSt amount around 3.2 mg/cm², for which a high

354 hydrophobicity contact angle (θ_A =143° ± 3°, θ_R = 135° ± 9°) is complemented by a transmittance of 25%.

355
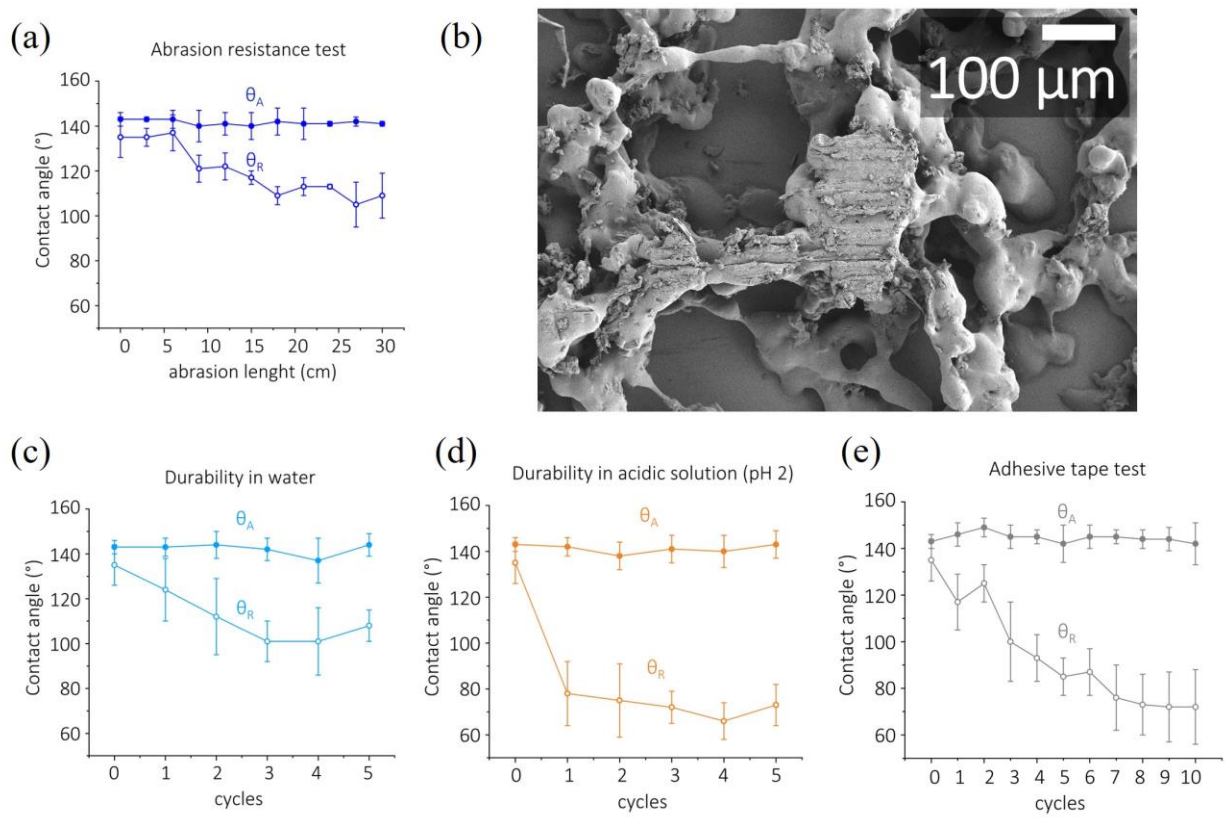
Fig. 6. Durability assessment of 3.2 mg/cm² samples, θ_A (closed circles) and θ_R (open circles). (a) Abrasion resistance test. (b) SEM analysis of the coating after the abrasion test. (c) Durability test in water. (d) Durability test in acidic solution (pH 2). (e) ISO standard adhesive tape test (EN ISO 2409).

359 To assess coating abrasion resistance, a simple in-house abrasion test was implemented, using sandpaper. The

360 evolution of advancing and receding contact angles was monitored for cumulative abrasion length of 30 cm. The

361 sample was pulled face down over sandpaper, with a 100 g weight on top of it to ensure constant pressure of 1.6 kPa

362 on the sample area. As visible in Fig. 6a, the θ_A remains almost constant over the entire test, whereas the θ_R decreases

363 from 143° ± 3° to 109° ±10° at 30 cm. As such, the durability can be considered good, as the coating remains

364 hydrophobic; nonetheless, the increase of $\Delta\theta$ reduces the self-cleaning performance of the surface, with an increase of

365 the roll-off angle. The samples were analyzed by SEM after the abrasion test (Fig. 6b). Over the surface it is possible

366 to find abrasion signs, but the overall structure is well maintained, showing good resistance over physical abrasion.

367 The resistance of the coating has been evaluated also in water (pH 6.5) and acidic solution (pH 2) (Fig. 6c,d)(Malavasi

368 et al., 2015). For both cases, the θ_A remains almost constant over the entire test consisting of 5 cycles of immersion in

369 the solution and drying in the air. In the case of the test in water, the θ_R decreases from $135° \pm 9°$ to $108° \pm 7°$. During

370 the first 3 cycles θ_R decreases linearly reaching a plateau after cycle 3. In the case of the acidic solution, the θ_R

371 significantly decreases in the first cycle from $135° \pm 9°$ to $78° \pm 14°$, and then remain constants after additional cycles.

372 The coating thus remains hydrophobic in both water and very acidic environment, although with an increase in $\Delta\theta$,

373 which impact on roll-off angle and self-cleaning performances. The ChiSt coating proved not to dissolve in water and

374 acidic conditions as demonstrated by the quasi-static contact angle analysis, where θ_A remains almost constant along

375 the durability assessment. In the case of coating dissolution, θ_A would have reached quickly the value of bare glass.

376 On the other hand, the θ_R decrease may be due to partial particles detachment from the glass substrate.

377 At last, the coating adhesion to the surface is tested by ISO standard adhesive tape test (EN ISO 2409) (Maitra et al.,

378 2014) as shown in Fig. 6e. Also in this case, the θ_A is very stable at 140°-145°, while the θ_R decreases from $135° \pm 9°$

379 to $70° ° \pm 10°$ after 7 cycles, and then remains constant. The coating proved to be anchored to the surface, even though

380 the repeated cycles of adhesion tests determined an increase of hysteresis which alters water repellency efficiency.

381 Being a bio-based coating, an ideal real-use application could make use of repeated deposition over time for

382 maximizing hydrophobicity. Future studies will be devoted to further improve the coating adhesion resistance and

383 durability.

384 **3. Conclusion**

385 In summary, in this study a safe and sustainable fluorine-free coating is developed using chitosan, which is first

386 modified with fatty acid side groups and then deposited through a solvent-free deposition method. The chitosan

387 functionality effective modification with stearoyl groups is assessed and confirmed via combined by ^{1}H and ^{13}C DD-

388 MAS Solid State NMR, FTIR and TGA analysis. The modified chitosan has been freeze-dried to allow safe long-term

389 storage, sieved and thermally treated to create a coating. A superhydrophobic wetting state ($\theta_A = 150°$, $\theta_R = 144°$) was

390 reached for coating with ChiSt amount of 4.8 mg/cm^2. An optimal balance of hydrophobicity and transparency was

391 assessed for ChiSt amount 3.2 mg/cm^2 ($\theta_A = 143°$, $\theta_R = 135°$), showing good durability in abrasion resistance tests, in

392 water and acidic environment and over adhesion tape tests.

393 Our innovative and sustainable deposition method for modified chitosan is a simple procedure for creating transparent

394 hydrophobic coatings, which are fluorine-free and do not require any solvent during deposition. As an outlook, we

395 envision a further coating development to better control surface topography, with the goal of decreasing light scattering

396 and increasing transmittance and improving mechanical durability using adhesion promoters or cross-linkers.

397 In perspective, our study will prompt the design of novel polysaccharide-based, bio-derived materials as an alternative

398 to the traditional oil-based polymers, contributing to a more sustainable and circular economy.

405 **5. Supporting Information.**

406 Video SV1. Superhydrophobic properties of freeze-dried ChiSt powder (mp4).

407 Fig. S1 HP-SEC-TDA of chitosan. Fig. S2. ^{1}H-NMR spectra of chitosan. Fig. S3. ^{1}H-NMR spectra of hydrolyzed

408 ChiSt in CDCl$_3$. Fig. S4. UV-Vis spectra of ChiSt coatings deposited on glass slides. Fig. S5. SEM evaluation of the

409 thickness (a) 0.8 mg/cm^2, (b) 1.6 mg/cm^2, (c) 3.2 mg/cm^2, d) 4.8 mg/cm^2. Fig. S6. DSC analysis of chitosan, ChiSt

410 and ChiSt after the temperature treatment. The analysis was carried at a heating rate of 20°C/ min with a ramp from

411 25°C to 200°C, 2 minutes of delay, from 200°C to 25°C, 2 minutes of delay, from 25°C to 250°C. Fig. S7. TGA

412 analysis comprising thermal degradation of Stearoyl chloride, chitosan, ChiSt, ChiSt after the temperature treatment

413 (pdf).

414 **6. Declaration of competing interest**

415 The authors declare that they have no known competing financial interests or personal relationships that could have

416 appeared to influence the work reported in this paper.

7. REFERENCES

Ajadi, D. A., Agboola, S. M., & Adedokun, O. (2016). Effect of Spin Coating Speed on Some Optical Properties of ZnO Thin Films. *Journal of Materials Science and Chemical Engineering*, *04*(05), 1–6. https://doi.org/10.4236/msce.2016.45001

Alkan, C., Sari, A., & Biçer, A. (2012). Thermal energy storage by poly(styrene-co-p-stearoylstyrene) copolymers produced by the modification of polystyrene. *Journal of Applied Polymer Science*, *125*(5), 3447–3455. https://doi.org/10.1002/app.36527

Antonini, C., Villa, F., Bernagozzi, I., Amirfazli, A., & Marengo, M. (2013). Drop rebound after impact: The role of the receding contact angle. *Langmuir*, *29*(52), 16045–16050. https://doi.org/10.1021/la4012372

Asmone, A. S., & Chew, M. Y. L. (2018). An investigation of superhydrophobic self-cleaning applications on external building façade systems in the tropics. *Journal of Building Engineering*, *17*, 167–173. https://doi.org/10.1016/j.jobe.2018.02.011

Bayer, I. S. (2020). Superhydrophobic Coatings from Ecofriendly Materials and Processes: A Review. *Advanced Materials Interfaces*, *7*(13), 1–25. https://doi.org/10.1002/admi.202000095

Butt, H. J., Roisman, I. v., Brinkmann, M., Papadopoulos, P., Vollmer, D., & Semprebon, C. (2014). Characterization of super liquid-repellent surfaces. In *Current Opinion in Colloid and Interface Science* (Vol. 19, Issue 4, pp. 343–354). Elsevier Ltd. https://doi.org/10.1016/j.cocis.2014.04.009

Caporale, N., Leemans, M., Birgersson, L., Germain, P.-L., Cheroni, C., Borbély, G., Engdahl, E., Lindh, C., Bressan, R. B., Cavallo, F., Chorev, N. E., D'Agostino, G. A., Pollard, S. M., Rigoli, M. T., Tenderini, E., Tobon, A. L., Trattaro, S., Troglio, F., Zanella, M., … Testa, G. (2022). From cohorts to molecules: Adverse impacts of endocrine disrupting mixtures. *Science*, *375*(6582). https://doi.org/10.1126/science.abe8244

Cazón, P., Velazquez, G., Ramírez, J. A., & Vázquez, M. (2017). Polysaccharide-based films and coatings for food packaging: A review. *Food Hydrocolloids*, *68*, 136–148. https://doi.org/10.1016/j.foodhyd.2016.09.009

Chen, L., Geissler, A., Bonaccurso, E., & Zhang, K. (2014). Transparent slippery surfaces made with sustainable porous cellulose lauroyl ester films. *ACS Applied Materials and Interfaces*, *6*(9), 6969–6976. https://doi.org/10.1021/am5020343

443   Chen, X., Huang, Y., Zhang, L., Liu, J., Wang, C., & Wu, M. (2022). Cellulose nanofiber assisted dispersion of

444   hydrophobic SiO2 nanoparticles in water and its superhydrophobic coating. *Carbohydrate Polymers*, 119504.

445   https://doi.org/https://doi.org/10.1016/j.carbpol.2022.119504

446   Commission Delegated Regulation (EU) 2020/784 of 8 April 2020 amending Annex I to Regulation (EU) 2019/1021

447   of the European parliament and of the Council as regards the listing of perfluorooctanoic acid (PFOA), its salts

448   and PFOA-related compounds, (2020).

449   Commission Regulation (EU) 2017/1000 of 13 June 2017 amending Annex XVII to Regulation (EC) No 1907/2006

450   of the European Parliament and of the Council concerning the Registration, Evaluation, Authorisation and

451   Restriction of Chemicals (REACH), (2017). http://echa.europa.eu/documents/10162/e9cddee6-3164-473d-

452   b590-8fcf9caa50e7

453   Divandari, M., Arcifa, A., Ayer, M. A., Letondor, C., & Spencer, N. D. (2021). Applying an Oleophobic/Hydrophobic

454   Fluorinated Polymer Monolayer Coating from Aqueous Solutions. *Langmuir*, *37*(14), 4387–4394.

455   https://doi.org/10.1021/acs.langmuir.1c00479

456   Donati, M., Lam, C. W. E., Milionis, A., Sharma, C. S., Tripathy, A., Zendeli, A., & Poulikakos, D. (2021). Sprayable

457   Thin and Robust Carbon Nanofiber Composite Coating for Extreme Jumping Dropwise Condensation

458   Performance. *Advanced Materials Interfaces*, *8*(1). https://doi.org/10.1002/admi.202001176

459   Dong, Y., Ruan, Y., Wang, H., Zhao, Y., & Bi, D. (2004). Studies on glass transition temperature of chitosan with

460   four techniques. *Journal of Applied Polymer Science*, *93*(4), 1553–1558. https://doi.org/10.1002/app.20630

461   Duan, C., Meng, X., Meng, J., Khan, M. I. H., Dai, L., Khan, A., An, X., Zhang, J., Huq, T., & Ni, Y. (2019). Chitosan

462   as A Preservative for Fruits and Vegetables: A Review on Chemistry and Antimicrobial Properties. *Journal of*

463   *Bioresources and Bioproducts*, *4*(1), 11–21. https://doi.org/10.21967/jbb.v4i1.189

464   Eral, H. B., 'T Mannetje, D. J. C. M., & Oh, J. M. (2013). Contact angle hysteresis: A review of fundamentals and

465   applications. *Colloid and Polymer Science*, *291*(2), 247–260. https://doi.org/10.1007/s00396-012-2796-6

466   Eriksson, M., Tuominen, M., Järn, M., Claesson, P. M., Wallqvist, V., Butt, H. J., Vollmer, D., Kappl, M., Schoelkopf,

467   J., Gane, P. A. C., Teisala, H., & Swerin, A. (2019). Direct observation of gas meniscus formation on a

468   superhydrophobic surface. *ACS Nano*, *13*(2), 2246–2252. https://doi.org/10.1021/acsnano.8b08922

469   Fernandes, S. C. M., Oliveira, L., Freire, C. S. R., Silvestre, A. J. D., Neto, C. P., Gandini, A., & Desbriéres, J. (2009).

470   Novel transparent nanocomposite films based on chitosan and bacterial cellulose. *Green Chemistry*, *11*(12),

471   2023–2029. https://doi.org/10.1039/b919112g

472   Fink, K., Höhne, S., Spange, S., & Simon, F. (2009). Hydrophobically functionalized chitosan particles. *Journal of*

473   *Adhesion Science and Technology*, *23*(2), 297–315. https://doi.org/https://doi.org/10.1163/156856108X388399

474   Geissler, A., Chen, L., Zhang, K., Bonaccurso, E., & Biesalski, M. (2013). Superhydrophobic surfaces fabricated from

475   nano- and microstructured cellulose stearoyl esters. *Chemical Communications*, *49*(43), 4962–4964.

476   https://doi.org/10.1039/c3cc41568f

477   Geyer, F., D'Acunzi, M., Sharifi-Aghili, A., Saal, A., Gao, N., Kaltbeitzel, A., Sloot, T. F., Berger, R., Butt, H. J., &

478   Vollmer, D. (2020). When and how self-cleaning of superhydrophobic surfaces works. *Science Advances*, *6*(3),

479   1–12. https://doi.org/10.1126/sciadv.aaw9727

480   Ghasemlou, M., Le, P. H., Daver, F., Murdoch, B. J., Ivanova, E. P., & Adhikari, B. (2021). Robust and Eco-Friendly

481   Superhydrophobic Starch Nanohybrid Materials with Engineered Lotus Leaf Mimetic Multiscale Hierarchical

482   Structures. *ACS Applied Materials and Interfaces*, *13*(30), 36558–36573.

483   https://doi.org/10.1021/acsami.1c09959

484   Han, X., Zheng, Z., Yu, C., Deng, Y., Ye, Q., Niu, F., Chen, Q., Pan, W., & Wang, Y. (2022). Preparation,

485   characterization and antibacterial activity of new ionized chitosan. *Carbohydrate Polymers*, *290*, 119490.

486   https://doi.org/10.1016/j.carbpol.2022.119490

487   Heale, F. L., Page, K., Wixey, J. S., Taylor, P., Parkin, I. P., & Carmalt, C. J. (2018). Inexpensive and non-toxic water

488   repellent coatings comprising SiO2 nanoparticles and long chain fatty acids. *RSC Advances*, *8*(48), 27064–

489   27072. https://doi.org/10.1039/c8ra04707c

490   Hokmabad, B. V., & Ghaemi, S. (2017). Effect of Flow and Particle-Plastron Collision on the Longevity of

491   Superhydrophobicity. *Scientific Reports*, *7*, 1–10. https://doi.org/10.1038/srep41448

492   Huang, J., Wang, S., Lyu, S., & Fu, F. (2018). Preparation of a robust cellulose nanocrystal superhydrophobic coating

493   for self-cleaning and oil-water separation only by spraying. *Industrial Crops and Products*, *122*(December

494   2017), 438–447. https://doi.org/10.1016/j.indcrop.2018.06.015

495   Huang, J., Yang, M., Zhang, H., & Zhu, J. (2021). Solvent-Free Fabrication of Robust Superhydrophobic Powder

496   Coatings. *ACS Applied Materials and Interfaces*, *13*(1), 1323–1332. https://doi.org/10.1021/acsami.0c16582

497   Huang, Z., Gurney, R. S., Wang, Y., Han, W., Wang, T., & Liu, D. (2019). TDI/TiO 2 Hybrid Networks for

498   Superhydrophobic Coatings with Superior UV Durability and Cation Adsorption Functionality. *ACS Applied*

499   *Materials and Interfaces*, *11*(7), 7488–7497. https://doi.org/10.1021/acsami.9b00886

500   Jaber, N., Al-Remawi, M., Al-Akayleh, F., Al-Muhtaseb, N., Al-Adham, I. S. I., & Collier, P. J. (2022). A review of

501   the antiviral activity of Chitosan, including patented applications and its potential use against COVID-19. In

502   *Journal of Applied Microbiology* (Vol. 132, Issue 1, pp. 41–58). John Wiley and Sons Inc.

503   https://doi.org/10.1111/jam.15202

504   Jiang, R., Hao, L., Song, L., Tian, L., Fan, Y., Zhao, J., Liu, C., Ming, W., & Ren, L. (2020). Lotus-leaf-inspired

505   hierarchical structured surface with non-fouling and mechanical bactericidal performances. *Chemical*

506   *Engineering Journal*, *398*, 125609. https://doi.org/10.1016/j.cej.2020.125609

507   Junaidi, M. U. M., Ahmad, N. N. R., Leo, C. P., & Yee, H. M. (2016). Near superhydrophobic coating synthesized

508   from rice husk ash: Anti-fouling evaluation. *Progress in Organic Coatings*, *99*, 140–146.

509   https://doi.org/10.1016/j.porgcoat.2016.05.018

510   Khodayari, A., Hirn, U., van Vuure, A. W., & Seveno, D. (2020). Inverse rule of mixtures at the nanoscale: Prediction

511   of elastic properties of cellulose nanofibrils. *Composites Part A: Applied Science and Manufacturing*, *138*.

512   https://doi.org/10.1016/j.compositesa.2020.106046

513   Khodayari, A., Thielemans, W., Hirn, U., van Vuure, A. W., & Seveno, D. (2021). Cellulose-hemicellulose

514   interactions - A nanoscale view. *Carbohydrate Polymers*, *270*, 118364.

515   https://doi.org/10.1016/j.carbpol.2021.118364

516   Konrad, W., Ebner, M., Miranda, T., Thielen, S., & Nebelsick, J. H. (2022). When rain collides with plants-patterns

517   and forces of drop impact and how leaves respond to them. *Journal of Experimental Botany*, *erac004*.

518   https://doi.org/10.1093/jxb/erac004/6509732

519   Ladiè, R., Cosentino, C., Tagliaro, I., Antonini, C., Bianchini, G., & Bertini, S. (2021). Supramolecular structuring of

520   hyaluronan-lactose-modified chitosan matrix: Towards high-performance biopolymers with excellent

521   biodegradation. *Biomolecules*, *11*(3), 1–19. https://doi.org/10.3390/biom11030389

522   Lafuma, A., & Quéré, D. (2003). Superhydrophobic states. *Nature Materials*, *2*(7), 457–460.

523   https://doi.org/10.1038/nmat924

524   Levkin, P. A., Svec, F., & Fréchet, J. M. J. (2009). Porous polymer coatings: A versatile approach to superhydrophobic

525   surfaces. *Advanced Functional Materials*, *19*(12), 1993–1998. https://doi.org/10.1002/adfm.200801916

526   Li, D., Xu, W., Cheng, H., Xi, K., Xu, B., & Jiang, H. (2020). One-Step Thermochemical Conversion of Biomass

527   Waste into Superhydrophobic Carbon Material by Catalytic Pyrolysis. *Global Challenges*, *4*(4), 1900085.

528   https://doi.org/10.1002/gch2.201900085

529   Li, W., & Amirfazli, A. (2005). A thermodynamic approach for determining the contact angle hysteresis for

530   superhydrophobic surfaces. *Journal of Colloid and Interface Science*, *292*(1), 195–201.

531   https://doi.org/10.1016/j.jcis.2005.05.062

532   Liu, S., Zhang, X., & Seeger, S. (2019). Solvent-Free Fabrication of Flexible and Robust Superhydrophobic

533   Composite Films with Hierarchical Micro/Nanostructures and Durable Self-Cleaning Functionality. *ACS*

534   *Applied Materials and Interfaces*, *11*(47), 44691–44699. https://doi.org/10.1021/acsami.9b15318

535   Long, C., Qing, Y., Long, X., Liu, N., Xu, X., An, K., Han, M., Li, S., & Liu, C. (2022). Synergistic reinforced

536   superhydrophobic paper with green, durability, and antifouling function. *Applied Surface Science*, *579*.

537   https://doi.org/10.1016/j.apsusc.2021.152144

538   Madeleine-Perdrillat, C., Karbowiak, T., Debeaufort, F., Delmotte, L., Vaulot, C., & Champion, D. (2016). Effect of

539   hydration on molecular dynamics and structure in chitosan films. *Food Hydrocolloids*, *61*, 57–65.

540   https://doi.org/10.1016/j.foodhyd.2016.04.035

541   Mail, M., Moosmann, M., Häger, P., & Barthlott, W. (2019). Air retaining grids-a novel technology to maintain stable

542   air layers under water for drag reduction. *Philosophical Transactions of the Royal Society A: Mathematical,*

543   *Physical and Engineering Sciences*, *377*(2150). https://doi.org/10.1098/rsta.2019.0126

544   Maitra, T., Antonini, C., Auf Der Mauer, M., Stamatopoulos, C., Tiwari, M. K., & Poulikakos, D. (2014).

545   Hierarchically nanotextured surfaces maintaining superhydrophobicity under severely adverse conditions.

546   *Nanoscale*, *6*(15), 8710–8719. https://doi.org/10.1039/c4nr01368a

547   Malavasi, I., Bernagozzi, I., Antonini, C., & Marengo, M. (2015). Assessing durability of superhydrophobic surfaces.

548   *Surface Innovations*, *3*(1), 49–60. https://doi.org/10.1680/si.14.00001

549   Meng, L., Li, S., Yang, W., Simons, R., Yu, L., & Chen, Y. (2022). Enhancing water resistance of interface between

550   starch films and acrylated epoxidized soybean oil coating. *Progress in Organic Coatings*, *163*.

551   https://doi.org/10.1016/j.porgcoat.2021.106646

552   Milne, A. J. B., & Amirfazli, A. (2009). Drop shedding by shear flow for hydrophilic to superhydrophobic surfaces.

553   *Langmuir*, *25*(24), 14155–14164. https://doi.org/10.1021/la901737y

554   Milne, A. J. B., & Amirfazli, A. (2012). The Cassie equation: How it is meant to be used. In *Advances in Colloid and*

555   *Interface Science* (Vol. 170, Issues 1–2, pp. 48–55). https://doi.org/10.1016/j.cis.2011.12.001

556   Morin-Crini, N., Lichtfouse, E., Torri, G., & Crini, G. (2019). Applications of chitosan in food, pharmaceuticals,

557   medicine, cosmetics, agriculture, textiles, pulp and paper, biotechnology, and environmental chemistry.

558   *Environmental Chemistry Letters*, *17*(4), 1667–1692. https://doi.org/10.1007/s10311-019-00904-x

559   Morrissette, J. M., Carroll, P. J., Bayer, I. S., Qin, J., Waldroup, D., & Megaridis, C. M. (2018). A methodology to

560   produce eco-friendly superhydrophobic coatings produced from all-water-processed plant-based filler materials.

561   *Green Chemistry*, *20*(22), 5169–5178. https://doi.org/10.1039/c8gc02439a

562   Muñoz, I., Rodríguez, C., Gillet, D., & M. Moerschbacher, B. (2018). Life cycle assessment of chitosan production in

563   India   and   Europe.   *International   Journal   of   Life   Cycle   Assessment*,   *23*(5),   1151–1160.

564   https://doi.org/10.1007/s11367-017-1290-2

565   Muñoz-Bonilla, A., Bousquet, A., Ibarboure, E., Papon, E., Labrugère, C., & Rodríguez-Hernández, J. (2010).

566   Fabrication and superhydrophobic behavior of fluorinated microspheres. *Langmuir*, *26*(22), 16775–16781.

567   https://doi.org/10.1021/la102686y

568 Ostrov, I., Polishchuk, I., Shemesh, M., & Pokroy, B. (2019). Superhydrophobic Wax Coatings for Prevention of

569 Biofilm Establishment in Dairy Food. *ACS Applied Bio Materials*, *2*(11), 4932–4940.

570 https://doi.org/10.1021/acsabm.9b00674

571 Ouellette, R. J., & Rawn, J. D. (2018). Carboxylic Acids. In *Organic Chemistry* (pp. 625–663). Elsevier.

572 https://doi.org/10.1016/B978-0-12-812838-1.50021-9

573 Paxson, A. T., Yagüe, J. L., Gleason, K. K., & Varanasi, K. K. (2014). Stable dropwise condensation for enhancing

574 heat transfer via the initiated chemical vapor deposition (iCVD) of grafted polymer films. *Advanced Materials*,

575 *26*(3), 418–423. https://doi.org/10.1002/adma.201303065

576 Position (EU) No 14/2020 of the Council at first reading, (2020).

577 Queiroz, M. F., Melo, K. R. T., Sabry, D. A., Sassaki, G. L., & Rocha, H. A. O. (2015). Does the use of chitosan

578 contribute to oxalate kidney stone formation? *Marine Drugs*, *13*(1), 141–158.

579 https://doi.org/10.3390/md13010141

580 Quéré, D. (2005). Non-sticking drops. *Reports on Progress in Physics*, *68*(11), 2495–2532.

581 https://doi.org/10.1088/0034-4885/68/11/R01

582 Rayees, A. S., Maqsood, A. M., Shaeel, A. al-T., & Muneer, A. S. (2013). Chitosan as a Novel Edible Coating for

583 Fresh Fruits. *Food Science and Technology Research*, *19*(2), 139–155.

584 Ren, J., Tao, F., Lu, X., Zhang, H., Gai, L., Liu, L., & Jiang, H. (2021). Biomass-based superhydrophobic coating

585 with tunable colors and excellent robustness. *Carbohydrate Polymers*, *270*, 118401.

586 https://doi.org/10.1016/j.carbpol.2021.118401

587 Rinaudo, M. (2006). Chitin and chitosan: Properties and applications. *Progress in Polymer Science (Oxford)*, *31*(7),

588 603–632. https://doi.org/10.1016/j.progpolymsci.2006.06.001

589 Rioboo, R., Delattre, B., Duvivier, D., Vaillant, A., & de Coninck, J. (2012). Superhydrophobicity and liquid

590 repellency of solutions on polypropylene. In *Advances in Colloid and Interface Science* (Vol. 175, pp. 1–10).

591 Elsevier B.V. https://doi.org/10.1016/j.cis.2012.03.003

592   Saber-Samandari, S., Yilmaz, O., & Yilmaz, E. (2012). Photoinduced graft copolymerization onto chitosan under

593   heterogeneous conditions. *Journal of Macromolecular Science, Part A*, *49*(7), 591–598.

594   https://doi.org/https://doi.org/10.1080/10601325.2012.687970

595   Seth, M., & Jana, S. (2022). Development of superhydrophobic coating from biowaste and natural wax. *Materials*

596   *Today: Proceedings*. https://doi.org/https://doi.org/10.1016/j.matpr.2021.11.159

597   Soto, D., Ugur, A., Farham, T. A., Gleason, K. K., & Varanasi, K. K. (2018). Short-Fluorinated iCVD Coatings for

598   Nonwetting Fabrics.pdf. *Advanced Functional Materials*, *28*(1707355).

599   https://doi.org/https://doi.org/10.1002/adfm.201707355

600   Stokke, B., Varum, K. M., Holme, H. K., Hjerde, R. J. N., Smidsrsd, O., & Stokke, B. T. (1995). Sequence specificities

601   for lysozyme depolymerization of partially N-acetylated chitosans. *Canadian Journal of Chemistry*.

602   https://doi.org/https://doi.org/10.1139/v95-244

603   Tang, X., Huang, W., Xie, Y., Xiao, Z., Wang, H., Liang, D., Li, J., & Wang, Y. (2021). Superhydrophobic

604   Hierarchical Structures from Self-Assembly of Cellulose-Based Nanoparticles. *ACS Sustainable Chemistry and*

605   *Engineering*, *9*(42), 14101–14111. https://doi.org/10.1021/acssuschemeng.1c03876

606   Tanvir Ahmmed, K. M., & Kietzig, A. M. (2016). Drag reduction on laser-patterned hierarchical superhydrophobic

607   surfaces. *Soft Matter*, *12*(22), 4912–4922. https://doi.org/10.1039/c6sm00436a

608   Teisala, H., & Butt, H. J. (2019). Hierarchical Structures for Superhydrophobic and Superoleophobic Surfaces.

609   *Langmuir*, *35*(33), 10689–10703. https://doi.org/10.1021/acs.langmuir.8b03088

610   Vilaró, I., Yagüe, J. L., & Borrós, S. (2017). Superhydrophobic Copper Surfaces with Anticorrosion Properties

611   Fabricated by Solventless CVD Methods. *ACS Applied Materials & Interfaces*, *9*(1), 1057–1065.

612   https://doi.org/10.1021/acsami.6b12119

613   Wan, J., Xu, J., Zhu, S., Li, J., Wang, B., Zeng, J., Li, J., & Chen, K. (2021). Eco-Friendly Superhydrophobic

614   Composites with Thermostability, UV Resistance, and Coating Transparency. *ACS Applied Materials and*

615   *Interfaces*, *13*(51), 61681–61692. https://doi.org/10.1021/acsami.1c20419

616   Wang, F., Chang, R., Ma, R., & Tian, Y. (2021). Eco-friendly and superhydrophobic nano-starch based coatings for

617   self-cleaning application and oil-water separation. *Carbohydrate Polymers*, *271*, 118410.

618   https://doi.org/10.1016/j.carbpol.2021.118410

619   Wang, M., Zi, Y., Zhu, J., Huang, W., Zhang, Z., & Zhang, H. (2021). Construction of super-hydrophobic

620   PDMS@MOF@Cu mesh for reduced drag, anti-fouling and self-cleaning towards marine vehicle applications.

621   *Chemical Engineering Journal*, *417*, 129265. https://doi.org/10.1016/j.cej.2021.129265

622   Wang, Q., Zhang, B., Qu, M., Zhang, J., & He, D. (2008). Fabrication of superhydrophobic surfaces on engineering

623   material surfaces with stearic acid. *Applied Surface Science*, *254*(7), 2009–2012.

624   https://doi.org/10.1016/j.apsusc.2007.08.039

625   Wang, S., Sha, J., Wang, W., Qin, C., Li, W., & Qin, C. (2018). Superhydrophobic surfaces generated by one-pot

626   spray-coating of chitosan-based nanoparticles. *Carbohydrate Polymers*, *195*, 39–44.

627   https://doi.org/10.1016/j.carbpol.2018.04.068

628   Yang, J., Zhang, Z., Men, X., Xu, X., & Zhu, X. (2010). A simple approach to fabricate regenerable superhydrophobic

629   coatings. *Colloids and Surfaces A: Physicochemical and Engineering Aspects*, *367*(1–3), 60–64.

630   https://doi.org/10.1016/j.colsurfa.2010.06.016

631   Yazdani-Pedram, M., Lagos, A., Retuert, J., Guerrero, R., & Riquelme, P. (1995). On the modification of chitosan

632   through grafting. *Journal of Macromolecular Science, Part A: Pure and Applied Chemistry*, *32*(5), 1037–1047.

633   Yin, K., Divakar, P., & Wegst, U. G. K. (2019a). Freeze-casting porous chitosan ureteral stents for improved drainage.

634   *Acta Biomaterialia*, *84*, 231–241. https://doi.org/10.1016/j.actbio.2018.11.005

635   Yin, K., Divakar, P., & Wegst, U. G. K. (2019b). Plant-Derived Nanocellulose as Structural and Mechanical

636   Reinforcement of Freeze-Cast Chitosan Scaffolds for Biomedical Applications. *Biomacromolecules*, *20*(10),

637   3733–3745. https://doi.org/10.1021/acs.biomac.9b00784

638   Yin, K., Divakar, P., & Wegst, U. G. K. (2021). Structure-property-processing correlations of longitudinal freeze-cast

639   chitosan scaffolds for biomedical applications. *Journal of the Mechanical Behavior of Biomedical Materials*,

640   *121*, 104589. https://doi.org/10.1016/j.jmbbm.2021.104589

641   Zawadzki, J., & Kaczmarek, H. (2010). Thermal treatment of chitosan in various conditions. *Carbohydrate Polymers*,

642   *80*(2), 394–400. https://doi.org/10.1016/j.carbpol.2009.11.037

643   Zhang, Z. X., Li, Y., Ye, M., Boonkerd, K., Xin, Z., Vollmer, D., Kim, J. K., & Deng, X. (2014). Fabrication of

644   superhydrophobic surface by a laminating exfoliation method. *Journal of Materials Chemistry A*, *2*(5), 1268–

645   1271. https://doi.org/10.1039/c3ta14204c

646   Zhao, X., Li, Y., Li, B., Hu, T., Yang, Y., Li, L., & Zhang, J. (2019). Environmentally benign and durable

647   superhydrophobic coatings based on SiO 2 nanoparticles and silanes. *Journal of Colloid and Interface Science*,

648   *542*, 8–14. https://doi.org/10.1016/j.jcis.2019.01.115

649   Zhu, H., Zhu, S., Jia, Z., Parvinian, S., Li, Y., Vaaland, O., Hu, L., & Li, T. (2015). Anomalous scaling law of strength

650   and toughness of cellulose nanopaper. *Proceedings of the National Academy of Sciences of the United States of*

651   *America*, *112*(29), 8971–8976. https://doi.org/10.1073/pnas.1502870112

652   Zong, Z., Kimura, Y., Takahashi, M., & Yamane, H. (2000). Characterization of chemical and solid state structures

653   of acylated chitosans. *Polymer*, *41*(3), 899–906. https://doi.org/10.1016/S0032-3861(99)00270-0

654